

This work was written as part of one of the author's official duties as an Employee of the United States Government and is therefore a work of the United States Government. In accordance with 17 U.S.C. 105, no copyright protection is available for such works under U.S. Law.

Public Domain Mark 1.0





<https://creativecommons.org/publicdomain/mark/1.0/>

Access to this work was provided by the University of Maryland, Baltimore County (UMBC) ScholarWorks@UMBC digital repository on the Maryland Shared Open Access (MD-SOAR) platform.

Please provide feedback

Please support the ScholarWorks@UMBC repository by emailing scholarworks-group@umbc.edu and telling us what having access to this work means to you and why it's important to you. Thank you.

Calibration of Maxar Constellation Over Libya-4 Site Using MAIAC Technique

Myungje Choi , Alexei Lyapustin , Yujie Wang, Compton J. Tucker , Maudood N. Khan , Frederick Policelli , Christopher S. R. Neigh , and Alfreda A. Hall

Abstract—The very high resolution commercial satellite constellation of Maxar offers unique opportunities for a wide range of Earth science research and applications. The key to their widespread and effective use is stable and consistent calibration. In this article, we characterized the long-term calibration trends and cross-calibration coefficients for the four Maxar satellites (GeoEye-1, QuickBird-2, WorldView-2, and WorldView-3) using the Multi-Angle Implementation of Atmospheric Correction (MAIAC) processing technique. Utilizing MAIAC Moderate Resolution Imaging Spectroradiometer (MODIS) atmosphere and surface products, we calculated top-of-atmosphere (TOA) reflectance for the Blue, Green, Red, and near-infrared, or “NIR1” (NIR) bands over the Libya-4 desert site. To ensure data consistency, we applied geometric normalization to account for variations in TOA reflectance arising from different view geometries. In addition, a spatial transfer technique was employed to increase the number of samples and yield more robust statistical trend analysis. Our analysis revealed that half of the bands exhibited statistically significant calibration trends. These trends were found to be 2–3 times higher in magnitude compared with those observed in the early Collection 6 MODIS. After detrending, Maxar sensors were cross-calibrated to MODIS Aqua, considered as a calibration standard. In this process, German Aerospace Center (DLR) Earth Sensing Imaging Spectrometer hyperspectral measurements were used for spectral conversion required to align Maxar with MODIS bands. The cross-calibration analysis shows that GeoEye-1, WorldView-2, and WorldView-3 were systematically higher than MODIS Aqua by 2%–4% in the Blue, Green, and NIR bands, and by 7%–8% in the Red band. Detrending and cross-calibration to MODIS Aqua effectively transforms the Maxar constellation into a common sensor system enhancing spatiotemporal coverage and broadening the potential range of applications.

Index Terms—Commercial satellites, cross calibration, Multi-Angle Implementation of Atmospheric Correction (MAIAC), radiometric calibration trend, very high resolution (VHR).

I. INTRODUCTION

THE capability to reliably image the Earth at submeter to a few meters spatial resolution from space presents unique opportunities for monitoring the Earth and advancing Earth system science. The very high resolution (VHR) imagery helps identify and study processes and phenomena unresolved by the global coarse resolution spaceborne Earth observing systems. One such commercial satellite constellation is operated by Maxar Technologies (formerly DigitalGlobe). Many Earth science applications based on VHR images have been summarized by Neigh et al. [1] attesting to the versatility and significance of this technology in advancing our understanding of the Earth system. Among the growing number of latest applications of the Maxar data is detection and systematic quantification of abundant nonforest trees with crowns greater than 3 m² in size in West Africa. These dryland trees store quantifiable amounts of carbon (0.54–3.7 Mg C ha^{−1}) but were not previously considered in desertification scenarios or climate and carbon models [2], [3]. Small-scale biomass and carbon stocks in forests [4], variety of ocean ecosystems and organisms [5], [6], and point sources of methane from industrial activities and fracking [7], [8], [9] were also discovered by using Maxar’s VHR satellites.

It is important to highlight that accurate long-term sensor calibration is critically important for the continuity and consistency of geophysical retrievals, and for maximizing the scientific return on investments. Maxar provides values of gain and offset for radiometric calibration of data converting recorded digital numbers to the top-of-atmosphere (TOA) radiance. The preflight calibration was performed using a full-aperture integrating sphere and NIST-traceable transfer radiometers, with the postlaunch adjustments through vicarious calibration campaigns [10], [11]. While Maxar’s ongoing vicarious calibration efforts primarily address significant shifts in the sensors’ calibration, individual calibration evaluation studies are limited to a few scenes comparisons [12]. In the absence of Sun- or Moon-based calibration, coincident underflight observations of the Earth in the same view geometry with well-calibrated reference satellite sensor offer a vicarious calibration opportunity [13], [14], [15]. Among its other tasks, the NASA Climate Absolute Radiance and Refractivity Observatory (CLARREO) pathfinder expected to be launched to the International Space Station (ISS) in 2024 will serve as an on-orbit reference for other satellite instruments and will demonstrate the capability to transfer its unparalleled high accuracy to other Earth-viewing satellites [16], [17].

Manuscript received 7 November 2023; revised 17 January 2024; accepted 4 February 2024. Date of publication 19 February 2024; date of current version 4 March 2024. “This work was supported by the NASA Commercial Smallsat Data Acquisition (CSDA) Program through Maxar and DESIS data.” (Corresponding authors: Alexei Lyapustin; Myungje Choi.)

Myungje Choi and Yujie Wang are with the University of Maryland, Baltimore, MD 21250 USA, and also with the NASA Goddard Space Flight Center, Greenbelt, MD 20771 USA (e-mail: myungje.choi@nasa.gov; yujie.wang-1@nasa.gov).

Alexei Lyapustin, Compton J. Tucker, Frederick Policelli, and Christopher S. R. Neigh are with the NASA Goddard Space Flight Center, Greenbelt, MD 20771 USA (e-mail: alexei.i.lyapustin@nasa.gov; compton.j.tucker@nasa.gov; frederick.s.policelli@nasa.gov; christopher.s.neigh@nasa.gov).

Maudood N. Khan is with the Booz Allen Hamilton at NASA Headquarters, Washington, DC 20546 USA.

Alfreda A. Hall, retired, was with the NASA Goddard Space Flight Center, Greenbelt, MD 20771 USA (e-mail: alfreda.a.hall@gmail.com).

Digital Object Identifier 10.1109/JSTARS.2024.3367250

An accurate characterization of the atmospheric state including column water vapor (CWV) and aerosol optical depth (AOD) along with spectral surface bidirectional reflectance distribution function (BRDF) over quasi-stable desert calibration sites offers an alternative opportunity for vicarious calibration. The NASA's Multi-Angle Implementation of Atmospheric Correction (MAIAC) algorithm provides daily global atmospheric and surface geophysical properties from the Moderate Resolution Imaging Spectroradiometer (MODIS) [18]. Knowledge of the atmospheric and surface state allows us to recompute the TOA reflectance of the sensor of interest in the normalized view geometry in order to assess calibration trends and to compare measurements from the same sensor on different space platforms. This technique has been originally developed to cross-calibrate MODIS Terra to a more stable and predictable MODIS Aqua [19] and used in the MODIS Land discipline reprocessing starting with Collection 6. Recently, this technique was generalized to account for different relative spectral response (RSR) of sensors and applied to cross-calibrate Visible Infrared Imaging Radiometer Suite (VIIRS) on SNPP and NOAA-20 satellites to MODIS Aqua considered as a calibration standard [20], thus ensuring consistency and continuity of the MODIS-initiated climate data records in the VIIRS era.

In this study, we applied MAIAC-based vicarious calibration technique to four VHR satellites of the Maxar constellation, GeoEye-1 (GE1), QuickBird-2 (QB2), WorldView-2 (WV2), and WorldView-3 (WV3). We characterized the long-term calibration trends and cross-calibrated sensors to MODIS Aqua. The rest of this article is organized as follows. Section II gives a brief introduction of NASA Commercial Smallsat Data Acquisition (CSDA) Program, which supported this work. Section III describes Maxar and ancillary datasets used in the analysis. Section IV provides description of methods employed, results of calibration trend analysis, and cross-calibration for Maxar sensors to MODIS Aqua. Section V discusses the possible impact on applications. Finally, Section VI concludes this article.

II. NASA CSDA PROGRAM

This work was conducted as part of the NASA CSDA Program.¹ NASA's CSDA program was initially a pilot Private-Sector Small Constellation Satellite Data Product Pilot to identify, evaluate, and acquire data from commercial sources that support NASA's Earth science research and application goals. NASA's Earth Science Division recognizes that data from commercial systems have the potential to complement existing NASA data sources to advance Earth system science and applications development for societal benefit. The pilot transitioned into a sustained program in 2020 after demonstrating the usefulness of commercial data for advancing scientific research and applications. In 2021, CSDA expanded the end user licensing agreements to make the data more readily available across the US government and improve both value and interagency collaboration. The objectives of the NASA CSDA program are to establish a continuous and repeatable process

to onboard new commercial data vendors, enable sustained use and dissemination of purchased data by the Earth science community, ensure long-term data preservation, access, and distribution, and coordinate with other US government agencies and international partners on the evaluation and scientific use of commercial data. The NASA CSDA Program evaluates commercial data offerings according to the following criteria: data accessibility, metadata quality/completeness, user support, data utility for research and applications, and data quality, including calibration and geolocation.

III. DATASETS

A quasi-stable desert calibration/validation site of the Committee on Earth Observation Satellites (CEOS) working group for calibration and validation infrared and visible optical sensors centered at 28.55°N, 23.39°E, and commonly referred to as Libya-4² was used in this study. This desert location with sand dunes that lacks vegetation has low average atmospheric aerosol loading and experiences minimal rainfall providing rather homogeneous bright surface at scale of several kilometers and a long-term stability. Lyapustin et al. [19] analyzed seven different CEOS-recommended sites and excluded three (Niger, Sudan-1, and Mali-1) as they are not reliable for calibration analysis. The remaining four sites (Libya-1, Libya-2, Libya-4, and Egypt-1) produce very similar calibration results well represented by Libya-4.

For this work, we collected collocated datasets from Maxar, from German Aerospace Center (DLR) Earth Sensing Imaging Spectrometer (DESI), and from MAIAC MODIS over a $100 \times 100 \text{ km}^2$ area centered at Libya-4. The ancillary MODIS data are at 1-km resolution on the global sinusoidal grid. The Maxar and DESI data are initially aggregated to 1 km to match MODIS grid, and then superaggregated to $5 \times 5 \text{ km}^2$ for our analysis. The aggregation allows us to use the MAIAC MODIS atmospheric and surface ancillary data and ensures a good correspondence between Maxar imagery and MODIS Aqua BRDF within an $5 \times 5 \text{ km}^2$ area. It also removes high spatial resolution features, such as dune reflectance peaks and shadows, over the Libya-4, which is important in the cross-sensor analysis [21], [22], [23]. For instance, the surface variability, as measured by the standard deviation of Maxar data, is approximately 5%–6% from the average TOA reflectance in the blue–near-infrared, or “NIR1” (NIR) bands at 1-km aggregation and is further reduced to 3%–4% at 5-km aggregation. A description of the Maxar, DESI, and MAIAC datasets is provided below.

A. Maxar Dataset

Through the NASA CSDA program, we collected four Maxar VHR satellites datasets: GE1, QB2, WV2, and WV3. The core specifications of the Maxar imagers are summarized in Table I. They provide spatial resolution of 1.2–2.6 m for spectral bands, and nadir swath (frame size) within 13–18 km. In our analysis, we focused on four common bands named “Blue,” “Green,” “Red,” and “NIR”. RSRs for these bands are shown in Fig. 1.

¹[Online] Available: <https://www.earthdata.nasa.gov/esds/csd>

²[Online] Available: <https://calval.cr.usgs.gov/apps/Libya-4>

TABLE I
SPECIFICATION OF MAXAR CONSTELLATION SATELLITES ANALYZED IN THIS STUDY

Satellite	GE1	QB2	WV2	WV3
Instrument	GeoEye Imaging System	Ball Global Imaging System 2000	WorldView-100 camera	WorldView-100 camera
Orbit	Sun-synchronous, 10:30 AM descending node	Sun-synchronous, 10:00/10:30 AM descending node	Sun-synchronous, 10:30 AM descending node	Sun-synchronous, 10:30 AM descending node
Range of view zenith angle	Up to 60°	Up to 45°	Up to 30°	Up to 45°
Spatial resolution (ground sample distance at nadir) for visible – near-infrared bands	1.65 m at nadir 1.82 m at 20° off-nadir	2.62 m at nadir 2.90 m at 20° off-nadir	1.85 m at nadir 2.07 at 20° off-nadir	1.25 m at nadir 1.38 m at 20° off-nadir
Swath width at nadir	15.3–17.3 km	16.5–18 km	16.4 km	13.1 km
Operation period (year)	2008–current	2001–2014	2009–current	2014–current
No. of collected images and period for analysis	89 (2010–2018)	23 (2004–2014)	44 (2012–2018)	58 (2014–2018)

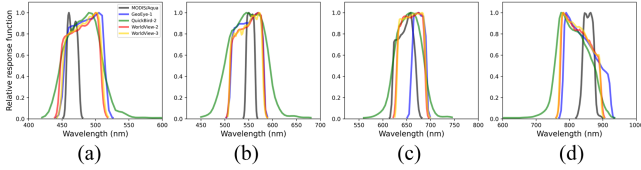


Fig. 1. RSRs of (a) Blue, (b) Green, (c) Red, and (d) NIR/NIR1 bands for Maxar satellites and corresponding RSRs of MODIS Aqua.

The width of Maxar RSRs is two to three times larger compared with the corresponding MODIS bands. While RSRs of WV2 and WV3 are very close, they differ considerably from GE1 and QB2.

B. MAIAC MODIS Ancillary Dataset of Atmospheric and Surface Properties

MAIAC is an interdisciplinary algorithm providing high-accuracy cloud/cloud shadow [24], [25] and snow detection [26], and CWV from MODIS NIR bands 17–19, AOD and atmospherically corrected spectral surface reflectance (SR), and BRDF [27], [28]. MAIAC atmospheric properties and BRDF are reported at 1-km spatial resolution on global sinusoidal grid in daily products MCD19A2 and MCD19A3, respectively. Both MAIAC AOD and CWV have an expected uncertainty of 10%–15% [18], [29], [30], [31], [32] based on regional and global validation against AERONET measurements [33]. A comparison of MAIAC SR with standard MODIS SR product MOD09 [34] showed that MAIAC provides from 5% to 25% more high-quality retrievals with improved accuracy in particular at the shortwave Blue–Green region [27]. For this work, we used MAIAC cloud/cloud shadow mask, AOD, CWV, and surface BRDF model parameters. With a wide swath of 2300 km, the two MODIS sensors on Terra and Aqua platforms provide daily global coverage and required ancillary information from MAIAC. The National Center for Environmental Predictions

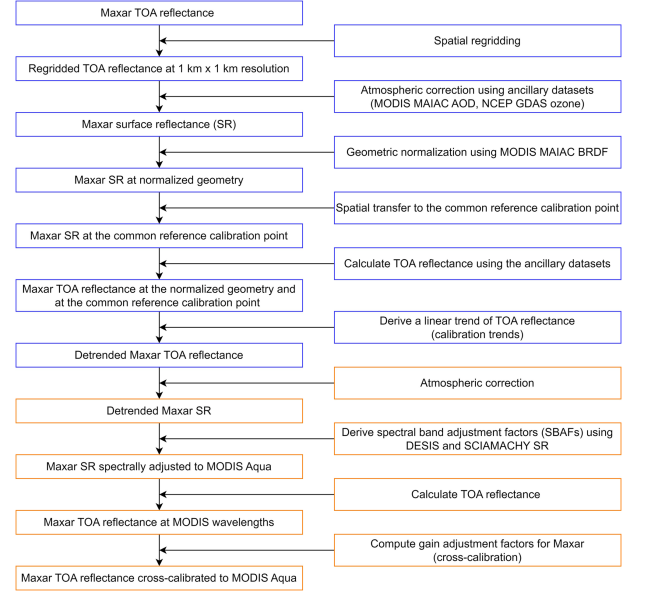


Fig. 2. Block diagram of calibration trend (blue blocks) and cross-calibration analyses (orange blocks).

(NCEP) Global Data Assimilation System’s total column ozone data at 1° resolution were used for ozone correction.

C. DESIS Hyperspectral SR

To account for differences in RSRs among Maxar imagers and MODIS and generate spectral band adjustment factors (SBAFs), we are using hyperspectral measurements of DLR DESIS. DESIS has been on board the ISS since 2018 and measures hyperspectral radiance reflected by Earth from 400 to 1000 nm with a spectral sampling of 2.55 nm and a full-width of half maximum of ~ 3.5 nm, with a total of 235 bands [35], [36]. The spatial resolution is 30 m with 1024 across-track pixels, resulting in a swath of ~ 30 km. Through the NASA CSDA program, we requested a systematic DESIS data acquisition over the Libya-4 site. In total, we manually selected 97 cloud-free good DESIS granules collected during 2018–2021. The bad quality pixels on the swath edges or in the middle of the scene affected by the stray light were filtered. In this study, we are using DESIS Level 2A SR version 2.13 product. It is worth noting that the DESIS SR is derived using the Lambertian assumption and is equivalent to Lambertian-equivalent reflectivity (LER).

IV. METHODS AND RESULTS

The block diagram (see Fig. 2) outlines the analysis procedures for assessing spectral calibration trends (blue blocks) and the subsequent cross-calibration to MODIS Aqua (orange blocks). At the top level, we initially aggregate Maxar TOA L1B data to MAIAC 1 km grid. Then, using MAIAC and NCEP ancillary dataset, we perform atmospheric correction of Maxar and compute scaling factor between MAXAR SR and MAIAC BRDF. Using scaled BRDF and atmospheric ancillary data, we recompute Maxar TOA reflectance in a fixed normalized view geometry with nadir view and Sun at 20° to assess the long-term

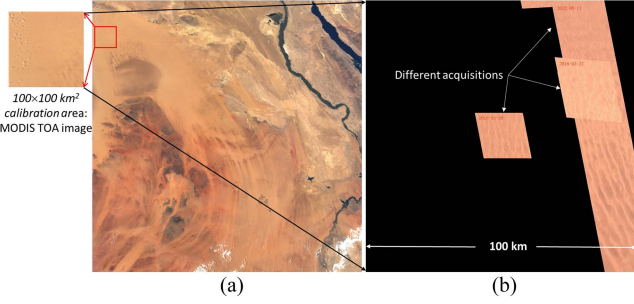


Fig. 3. (a) MODIS TOA true color image for tile H20V06. The inset shows selected $100 \times 100 \text{ km}^2$ calibration area centered at Libya-4. (b) WV2 data collection over enlarged $100 \times 100 \text{ km}^2$ calibration area.

linear calibration trends. With trends removed, and using SBAFs generated from DESIS, we recompute Maxar TOA reflectance but at the center wavelengths of MODIS Aqua reference bands in the normalized geometry. The ratio of spectrally shifted Maxar and MODIS Aqua TOA reflectance, both in the normalized view geometry, provides the gain adjustment factors for Maxar, or cross-calibration to MODIS. Details of the processing steps are provided below.

A. Calibration Trend Analysis

For this work, we generated MAIAC look-up tables (LUTs) for each of the four Maxar imagers using the combination of scalar radiative transfer code SHARM [37] and vector code IPOL [38]. Generated LUTs allow us to perform high-accuracy fast radiative transfer computations in arbitrary view geometry along with atmospheric correction [18], [39].

Contrary to MODIS and VIIRS, providing global daily coverage and significant statistics for calibration analysis, the small frame size of VHR imagery ($\sim 13\text{--}18 \text{ km}$) and target-based acquisition strategy of commercial systems severely limit the sampling statistics over our calibration site of interest. In order to increase the number of observations, we extended our analysis to a $100 \times 100 \text{ km}^2$ area centered at Libya-4. Fig. 3, left-hand side, shows an RGB image of the MODIS 1200 km tile H20V06 covering the north-eastern Africa. The marked north-western corner and the inset show the enhanced calibration area of the Libyan desert, which is relatively homogeneous and is well characterized by MAIAC MODIS. The right-hand side image shows different acquisitions of WV2 over the enhanced $100 \times 100 \text{ km}^2$ calibration area. To increase statistics, we employ geometric normalization and a novel “spatial transfer” technique both relying on MAIAC MODIS BRDF product.

The Maxar imagery was acquired at different view geometries with solar zenith angle (SZA) in the range $10^\circ\text{--}54^\circ$ and view zenith angle (VZA) $0^\circ\text{--}37^\circ$, including both forward- and back-scattering observation conditions. Geometric normalization to a common Sun and view geometry (nadir view and SZA of 20° , which is typical of those latitudes) reduces variance caused by the view geometry variations, which helps identify and characterize residual calibration trends left after the dedicated Sun, Moon, and vicarious calibration [19], [20]. Lyapustin et al. [19] found that geometric normalization reduces the variability of

reflectance at the bottom of the atmosphere by a factor of 2–5. The same approach applied to VIIRS showed that the estimated calibration trends agree with independent vicarious calibration results of both the MODIS/VIIRS characterization support team as well as the CERES Imager and Geostationary Calibration Group within an estimated uncertainty of 1%–2% [20]. Using MAIAC LUTs and MODIS/NCEP ancillary information (see Section III-B), we performed atmospheric correction of aggregated to 1 km Maxar data ($\rho_{\text{Maxar}}^{\text{meas}}$) and converted it to the common Sun and view geometry ($\rho_{\text{Maxar}}^{\text{norm}}$) using MAIAC MODIS BRDF. For each 1-km grid cell, MAIAC provides Lambertian, geometric, and volumetric kernel weights ($\mathbf{K} = \{k^L, k^G, k^V\}^T$) for the semiempirical Ross-thick Li-sparse (RTLS) BRDF model [40]. The RTLS model uses predefined geometric and volumetric kernels (f_G and f_V) depending on view geometry (θ_s, θ_v, ϕ —Sun and view zenith angles, and relative azimuth). The MODIS surface bidirectional reflectance factor (BRF) at the normalized view geometry can be expressed as $\rho_{\text{MODIS}}^{\text{norm}} = k^L(\lambda) + k^G(\lambda)f_G(\theta_s^n, \theta_v^n, \phi^n) + k^V(\lambda)f_V(\theta_s^n, \theta_v^n, \phi^n)$, where $\theta_s^n = 20^\circ$ and $\theta_v^n = 0^\circ$. Using these notations, the Maxar surface BRF_n in normalized view geometry is expressed as $\rho_{\text{Maxar}}^{\text{norm}} = \rho_{\text{Maxar}}^{\text{meas}} \left(\frac{\rho_{\text{MODIS}}^{\text{norm}}}{\rho_{\text{MODIS}}^{\text{meas}}} \right)$, where $\rho_{\text{MODIS}}^{\text{meas}}$ is computed at the view geometry of Maxar measurements.

Due to the small frame size of $\sim 17 \text{ km}$, there is little spatial overlap among the images collected over several years, in particular over the central location. To effectively increase the number of Maxar observations, we applied “spatial transfer” from each observation within selected $100 \times 100 \text{ km}^2$ area to a central reference point. In this step, we use Maxar data further aggregated to $5 \times 5 \text{ km}^2$ blocks to reduce the possible effect of surface inhomogeneity. We additionally require aggregated blocks to have at least 80% of concurrent high-quality MAIAC MODIS retrievals indicating mostly cloud-free and moderate-to-low AOD conditions. The transfer coefficient from any block to the center location is computed in the normalized geometry using MAIAC MODIS BRDF in the respective reference MODIS band, $T = \frac{\rho_{\text{MODIS}}^{\text{norm\¢er}}}{\rho_{\text{MODIS}}^{\text{norm}}}$, where numerator and denominator are computed using MAIAC MODIS BRDF parameters averaged over the $5 \times 5 \text{ km}^2$ areas at the center and at the given location, respectively. Here, we assume that the transfer coefficient based on the narrower MODIS bands adequately represents spatial variability in the respective wider Maxar bands. Spatial transfer allows us to effectively bring all available observations to center as follows: $\rho_{\text{Maxar}}^{\text{norm\¢er}} = \rho_{\text{Maxar}}^{\text{norm}} \left(\frac{\rho_{\text{MODIS}}^{\text{norm\¢er}}}{\rho_{\text{MODIS}}^{\text{norm}}} \right)$. Quantitatively, 651, 182, 364, and 116 blocks were produced from 89, 23, 44, and 58 images of GE1, QB2, WV2, and WV3 during 2010–2018, 2004–2014, 2012–2018, and 2014–2018, respectively. While different samples, generated from the same image from different $5 \times 5 \text{ km}^2$ blocks, strictly speaking, are not statistically independent, we still treat them as, such as, they help reduce the overall effect of uncertainties in the MODIS BRDF product.

Using Maxar surface BRF_n resulting from geometric normalization and spatial transfer, we compute scaling factor between BRF_n and average MODIS BRDF of the central block. Using the scaled BRDF, representing Maxar data, we finally compute the Maxar TOA reflectance in normalized geometry for each

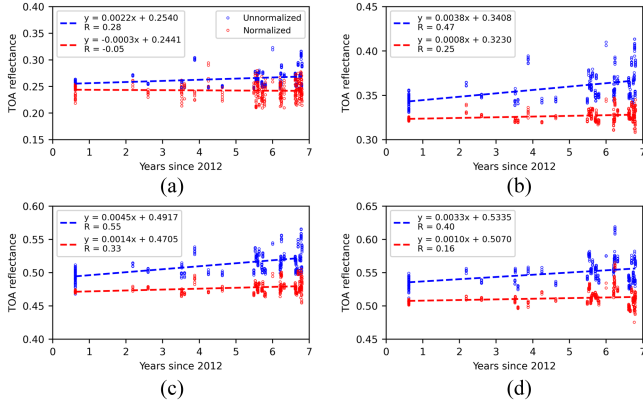


Fig. 4. Original (blue) and geometrically normalized (red) TOA reflectance trends of WV2 (a) Blue, (b) Green, (c) Red, and (d) NIR bands.

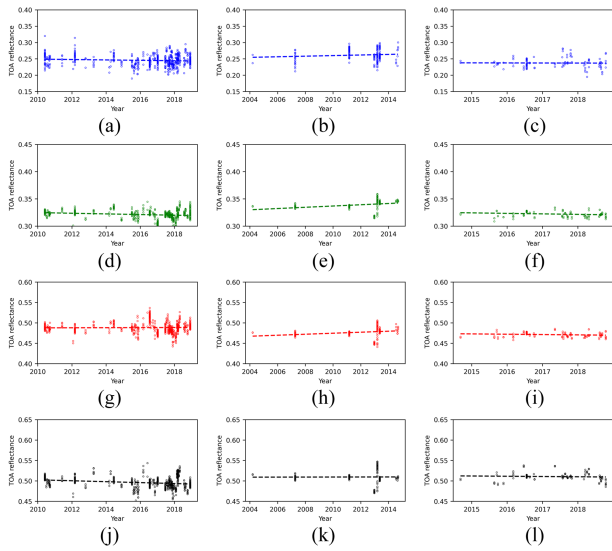


Fig. 5. TOA reflectance trends of GE1, QB2, and WV3.

$5 \times 5 \text{ km}^2$ sample using MAIAC LUTs and ancillary atmospheric data. Fig. 4 illustrates the time series of TOA reflectance for WV2 satellite showing data in both original and normalized geometry for spatially transferred blocks. One can immediately observe two features: 1) geometric normalization reduces variability, which is apparent in particular in the Green and Red bands, and 2) lack of geometric normalization would produce significantly larger unrealistic trends.

Fig. 5 shows time series of the normalized TOA reflectance for the other three Maxar satellites, GE1, QB2, and WV3, and the summary of the linear trend analysis is presented in Table II. The last column of this table gives the main result of trend analysis—trend per year per unit of reflectance. As a primer for the WV2 NIR band, the specified trend of 0.00188 per year per unit reflectance means that over 10 years, at a reflectance level of 0.5, the measured TOA signal will increase by 0.0094 or close to one absolute percent of reflectance.

We conducted Student's *t*-test to assess statistical significance of calibration trends at a 5% significance level. We also calculated the uncertainty of the trend using a 95% confidence

TABLE II
RESULTS OF TOA REFLECTANCE TREND ANALYSIS OF MAXAR SENSORS

Satellites	Bands	Calibration trend (/year) ($\times 1.0\text{E}-04$)	P-value	Is the trend significant? (Y or N)	95% CI low bound ($\times 1.0\text{E}-04$)	95% CI high bound ($\times 1.0\text{E}-04$)	SR (reference spot)	Normalized trend (/year/unit Refl.) ($\times 1.0\text{E}-04$)
GE1	Blue	-6.20	1.35E-02	Y	-11.1	-1.30	0.249	-24.8
	Green	-6.00	2.44E-06	Y	-8.50	-3.5	0.325	-18.5
	Red	1.08	6.03E-01	N	-3.00	5.15	0.488	2.21
	NIR	-11.3	1.96E-08	Y	-15.2	-7.4	0.503	-22.5
QB2	Blue	9.03	1.64E-01	N	-3.70	21.8	0.255	35.4
	Green	11.6	4.69E-04	Y	5.17	18.0	0.330	35.1
	Red	12.3	7.25E-03	Y	3.37	21.3	0.467	26.3
WV2	NIR	0.47	9.38E-01	N	-11.4	12.4	0.509	0.923
	Blue	-3.40	3.66E-01	N	-10.8	3.98	0.244	-13.9
	Green	7.68	2.00E-06	Y	4.55	10.8	0.323	23.9
	NIR	13.6	1.42E-10	Y	9.54	17.6	0.471	28.9
WV3	Blue	9.55	2.72E-03	Y	3.33	15.8	0.507	18.8
	Green	-2.20	8.77E-01	N	-30.5	26.1	0.238	-9.29
	Red	-9.30	5.84E-02	N	18.8	0.333	0.325	-28.4
	NIR	-8.00	1.49E-01	N	-18.9	2.9	0.474	-16.9
		-6.40	4.95E-01	N	24.8	12.1	0.513	-12.4

interval. The results indicate that half of the 16 investigated bands (four bands per satellite \times four satellites) exhibited significant calibration trends. Specifically, significant trends were observed in the Blue, Green, and NIR bands of GE1, the Green and Red bands of QB2, and the Green, Red, and NIR bands of WV2. In contrast, trends in analyzed bands of WV3 were found nonsignificant.

It is interesting to compare derived Maxar linear trends with results of the residual trend analysis for MODIS in early Collection 6. Lyapustin et al. [19] reported residual trends in both MODIS Terra and Aqua ranging from $-8.9\text{E}-4$ to $7.8\text{E}-4$ per year per unit reflectance for bands B3, B4, B1, and B2. Our current work indicates that the trends for Maxar sensors are approximately two to three times higher for most bands.

B. Maxar Cross-Calibration to MODIS Aqua

For sensors with similar RSRs (e.g., WV2 and WV3), the detrended TOA data are sufficient to compute cross-calibration factors as the ratio of offsets. In more generic case including ours, we need to account for the RSR differences resulting in shift of the effective center wavelength changing both surface and atmospheric contributions to TOA reflectance. In this work, MODIS Aqua is used as a calibration standard following our previous work of VIIRS calibration [20]. The radiometric calibration of MODIS's visible to shortwave infrared bands relies on several crucial elements, including solar diffuser (SD), SD stability monitor, periodic Moon observations during roll maneuvers, and trend removal based on monitoring of desert calibration sites with follow-on periodic application of more sensitive MAIAC-based detrending technique. These measures collectively contribute to maintaining the long-term stability of calibration, as discussed in previous works [19], [20], [41], [42], [43].

To account for the RSR differences between Maxar and MODIS Aqua and derive SBAFs for SR, we use the collected DESIS dataset. Cloud-free DESIS observations were averaged to $3 \times 3 \text{ km}^2$ for the central block to produce hyperspectral DESIS LER. The $3 \times 3 \text{ km}^2$ box was selected to increase the number of cloud-free DESIS scenes for our analysis. These data were verified against averaging to a $6 \times 6 \text{ km}^2$ resolution, which showed that the difference is negligible. Overall, spatial

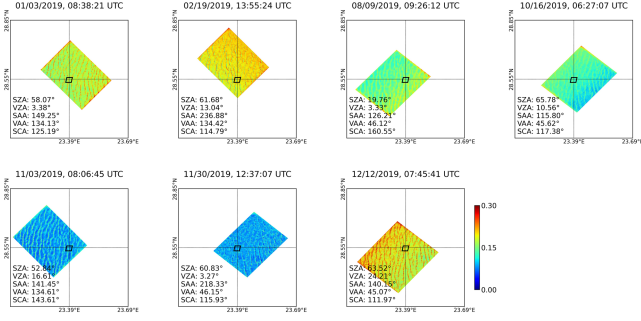


Fig. 6. Example of DESIS Level-2A surface LER at 402 nm, located at the central coordinates of the Libya-4 region (23.39°E, 28.55°N). The black diamond indicates the 3×3 km² averaging area. In each panel, view geometry is represented by SZA, view zenith angle (VZA), solar azimuth angle, view azimuth angle, and scattering angle.

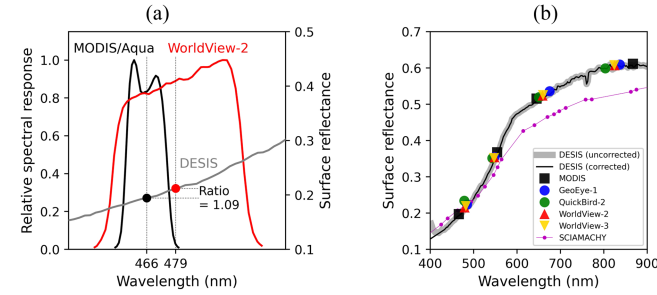


Fig. 7. (a) SBAF computation using DESIS measurements over Libya-4 on 3 January, 2019, 8:38:21 UTC. Band-integrated SR in MODIS (black dot) and WV2 (red dot) Blue bands is computed by convolution of hyperspectral DESIS LER (grey line) with MODIS Aqua and WV2 RSRs shown by black and red lines, respectively. (b) Geometrically normalized SR of DESIS, convolved to MODIS and Maxar satellite sensors, and SCIAMACHY climatology over Libya-4 site.

averaging helps mitigate uncertainties in geolocation and role of inhomogeneous sand dunes and their associated shadows, as illustrated in Fig. 6.

DESI LER was spectrally smoothed, mitigating spectral noise and correcting occasionally observed unphysical features, with the help of climatological Scanning Imaging Absorption spectroMeter for Atmospheric CartographY (SCIAMACHY) surface LER product [44]. The SCIAMACHY surface LER, derived from a decade of measurements (2002–2012) at a spatial resolution of $1^\circ \times 1^\circ$ provides a climatological perspective on spectral SR over Libya-4. DESIS spectra before and after correction are shown in Fig. 7(b) by gray and black lines. Next, smoothed DESIS LER (ρ_λ) was convolved to Maxar and reference MODIS band using RSRs and solar irradiance (E_λ), $\rho_{\text{simulated}} = \frac{\int_0^\infty \rho_\lambda E_\lambda \text{RSR}_\lambda d\lambda}{\int_0^\infty E_\lambda \text{RSR}_\lambda d\lambda}$.

We are using version 2 revision 1 Naval Research Laboratory's (NRL) solar irradiance model "NRLSSI2" [45]. The integral is evaluated using the trapezoidal rule. The ratio of computed Maxar and MODIS LERs provides SBAF, which is illustrated in Fig. 7(a), for the Blue band of MODIS Aqua (B3) and WV2 (SBAF = 1.09). Fig. 7(b) shows the average geometrically normalized SR for MODIS Aqua and for four Maxar sensors derived from DESIS. It is important to mention that MODIS LER simulated from DESIS agrees very well, within several

TABLE III
SBAF FOR MAXAR-TO-MODIS SR

Band names		Spectral conversion factors (Maxar/MODIS)			
MODIS Aqua	Maxar	GE1	QB2	WV2	WV3
B3 (466 nm)	Blue	1.105	1.159	1.073	1.088
B4 (554 nm)	Green	0.964	0.956	0.962	0.956
B1 (645 nm)	Red	1.044	1.009	0.934	0.924
B2 (867 nm)	NIR/NIR1	0.998	0.984	0.996	0.996

TABLE IV
MAXAR CROSS-CALIBRATION COEFFICIENTS TO THE REFERENCE MODIS AQUA

Band	GE1	QB2	WV2	WV3
Blue	1.0350	1.0194	1.0156	0.9956
Green	1.0290	1.1180	1.0343	1.0424
Red	1.0838	1.0959	1.0689	1.0799
NIR/NIR1	1.0267	1.0670	1.0189	1.0321

relative percent, with normalized reflectance generated from MAIAC MODIS BRDF product in the Blue–NIR wavelengths. This indicates that the calibration of DESIS and MODIS Aqua is very close [20] and we can reliably use DESIS to generate SBAFs for the Maxar imagers.

The final SBAFs, defined as the ratio of Maxar to MODIS, are presented in Table III. It should be mentioned that these numbers are specific to the Libya-4 site and cannot be used in other locations unless they have a similar SR spectrum.

With derived SBAFs, the calculation of cross-calibration coefficients between Maxar and MODIS Aqua is carried out as follows.

- 1) Detrended and geometrically normalized Maxar SR is obtained through atmospheric correction with MAIAC processing.
- 2) The Maxar SR is spectrally adjusted to match the MODIS Aqua reference wavelengths by applying SBAFs.
- 3) The geometrically normalized Maxar TOA reflectance is calculated next at the MODIS reference wavelength. The described spectral shift of Maxar SR and TOA computations at the same wavelength guarantee an apple-to-apple comparison between Maxar and MODIS.
- 4) Finally, the TOA reflectance ratio between the detrended and spectrally adjusted Maxar data and MODIS Aqua, both in normalized view geometry, provides gain adjustment (or cross-calibration) factor for Maxar.

Fig. 8 shows the TOA reflectance time series of geometrically normalized 1) detrended Maxar (blue), 2) detrended Maxar with spectral adjustment (red), and 3) MODIS Aqua (black). Spectral adjustment toward MODIS bands induces a distinct shift in the TOA reflectance, and the direction and magnitude of this shift vary depending on imager's bands. For instance, TOA reflectance decreases for the Blue bands of GE1, QB2, and WV3, and increases for the Green and Red bands. The Red band of GE1 shows a slight decrease, but QB2 and WV3 Red bands change little.

The derived Maxar cross-calibration coefficients are summarized in Table IV. The number of data points used to calculate these cross-calibration coefficients is 62, 5, 35, and 32 for GE1, QB2, WV2, and WV3, respectively. Due to very limited

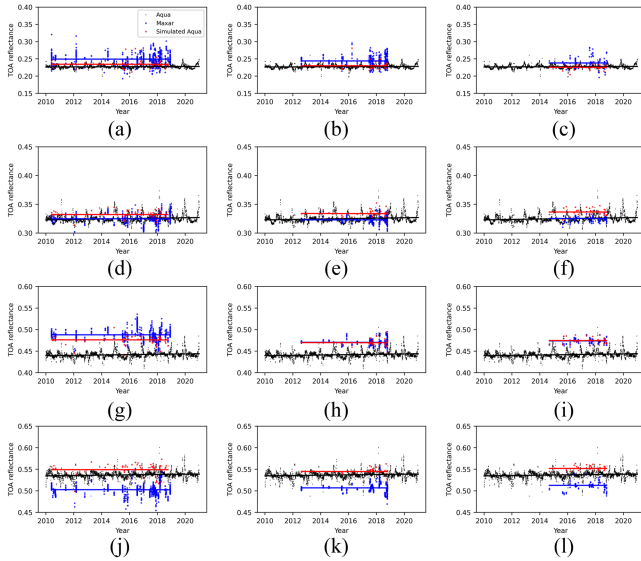


Fig. 8. TOA reflectance time series of normalized Maxar (GE1, WV2, and WV3) with consecutively applied detrending (blue) and spectral adjustment (red), and normalized MODIS Aqua (black).

sampling statistics for QB2, we do not consider these results reliable, and provide them only for the sake of comparison with other Maxar sensors. The cross-calibration coefficients for the other three Maxar sensors are relatively consistent, within approximately 2%–3% from each other. Except for the WV3 Blue band, which is nearly identical to MODIS Aqua B3, all sensors of Maxar constellation are calibrated higher than MODIS Aqua. Specifically, this results in higher TOA reflectance by about 2%–3% in the Blue and NIR bands, and 3%–4% in the Green band. The largest systematic difference of $\sim 7\%$ – 8% is found in the Red band.

V. DISCUSSIONS

This article presents a methodology and results of assessment of radiometric calibration trends in Maxar VHR satellites and of cross-calibration to the reference standard of MODIS Aqua. The conventional vicarious calibration involving ground-based measurements requires significant expenses to collect field data and is limited to accessible locations. On the contrary, the presented technique is automated and solves the problem of limited sampling in space and time from the very sparse coverage of VHR observations. Provided that SBAFs are available, it can be readily applied to any calibrated VHR satellite.

Given the limited accessibility of Maxar datasets, we could not find other reported studies evaluating their radiometric calibration. At the same time, our methodology of calibrating Terra to Aqua [19] has been proven by an extensive and successful use of the MODIS land discipline Collection 6 and 6.1 products in science analysis and applications. Similarly, our recent VIIRS SNPP and NOAA-20 to MODIS Aqua calibration [20] has demonstrated concurrence with other vicarious calibration

techniques involving deep convective clouds [46], [47], simultaneous overpass [48], [49], and pseudoinvariant bright surface targets including deserts and snow/ice (Antarctica Dome C) [50].

The reported calibration removes the long-term trends and harmonizes satellites of Maxar constellation resulting in improved consistency of derived geophysical properties. Importantly, cross-calibration to MODIS Aqua implies that spatially aggregated Maxar-derived geophysical products will align with the long-term global MODIS products, at least for the processes that can be approximated as linear in space. This opens a variety of possibilities, such as simulation of temporal gap filling of VHR observations using the coarse resolution (500 m to 1 km) MODIS as a constraint—an approach originally developed for Landsat [51]. Removal of calibration trends will increase Maxar’s usability for the analysis of the long-term trends and changes including those attributed to climate variability.

Ultimately, our methodology can be employed to create VHR mosaic images by integrating measurements from different periods and various sensors, including those within Maxar constellation but also between different constellations. Such approach would enhance spatiotemporal coverage beyond what individual satellites can achieve advancing our ability to monitor and understand dynamic Earth processes.

VI. CONCLUSION

The number of Earth monitoring VHR satellites from established and new constellations has been steadily increasing. While many of them still service operator-based image analyses applications, it is obvious that a consistent and systematic calibration of on-orbit VHR imagers could significantly increase their use in variety of application and science research. Here, we characterized calibration trends of the four Maxar imagers and cross-calibrated them to MODIS Aqua. Methodologically, geometrical normalization and spatial transfer were used over the quasi-stable Libya-4 desert region, combined with MAIAC MODIS processing, and atmospheric and surface BRDF products considered as ancillary data. The geometric normalization reduces variance from variations in view geometry, while spatial transfer technique helps increase the number of samples for statistical trend analysis and cross-calibration to MODIS. The cross-calibration from Maxar to MODIS Aqua relied on SBAFs derived from DESIS hyperspectral measurements.

Half of the Maxar bands of GE1 and WV2 reveal statistically significant calibration trends. Trends of WV3 were found non-significant, while the entire calibration analysis of QB2 cannot be considered reliable due to very small number of images available over the Libya-4 site. Overall, the calibration trends of Maxar are a factor of two to three times higher than those of the early Collection 6 MODIS. With exception of QB2, the Maxar images have a consistent calibration, within 2%–3% within each other. With exception of the Blue band of WV3, all Maxar imagers are calibrated systematically higher than MODIS Aqua producing higher TOA reflectance by about 2%–3% in the Blue and NIR bands, 3%–4% in the Green band, and $\sim 7\%$ – 8% in the Red band.

Finally, we recommend inclusion of Libya-4 in the list of mission-long preferred VHR acquisition targets, which would promote common calibration among VHR satellites traceable to the MODIS Aqua standard and expand user base of commercial vendors' data.

APPENDIX

List of Maxar Measurement Dates Utilized in this Study

Satellites	Measurement dates
GEI	5/31/2010, 6/30/2010, 7/14/2010, 7/30/2010, 9/4/2010, 9/15/2010, 6/3/2011, 1/25/2012, 3/3/2012, 10/17/2012, 4/8/2013, 3/10/2014, 4/6/2014, 6/13/2014, 11/24/2014, 7/4/2015, 7/7/2015, 8/9/2015, 8/17/2015, 8/20/2015, 9/5/2015, 9/19/2015, 9/22/2015, 9/27/2015, 11/2/2015, 11/5/2015, 11/10/2015, 11/13/2015, 11/16/2015, 11/24/2015, 3/4/2016, 6/2/2016, 7/21/2016, 8/9/2016, 9/27/2016, 10/16/2016, 11/4/2016, 11/7/2016, 11/10/2016, 12/26/2016, 1/6/2017, 6/18/2017, 7/15/2017, 8/9/2017, 8/20/2017, 9/8/2017, 9/13/2017, 9/16/2017, 9/19/2017, 9/24/2017, 10/16/2017, 11/1/2017, 11/4/2017, 11/7/2017, 11/15/2017, 11/23/2017, 12/12/2017, 12/15/2017, 1/25/2018, 2/2/2018, 2/24/2018, 3/4/2018, 3/7/2018, 3/12/2018, 3/15/2018, 3/18/2018, 4/3/2018, 4/22/2018, 7/24/2018, 8/7/2018, 8/23/2018, 10/6/2018, 12/2/2018
QB2	3/14/2004, 4/7/2007, 2/28/2011, 12/19/2012, 3/11/2013, 5/12/2013, 7/16/2014, 8/23/2014, 9/6/2014
WV2	8/11/2012, 3/7/2014, 8/6/2014, 7/5/2015, 7/8/2015, 8/4/2015, 11/13/2015, 3/30/2016, 8/15/2016, 6/25/2017, 7/9/2017, 7/17/2017, 7/28/2017, 8/5/2017, 8/16/2017, 9/12/2017, 9/17/2017, 9/23/2017, 10/9/2017, 10/17/2017, 12/30/2017, 3/13/2018, 3/16/2018, 3/21/2018, 3/24/2018, 3/27/2018, 4/23/2018, 8/10/2018, 8/15/2018, 8/18/2018, 8/26/2018, 9/9/2018, 9/22/2018, 9/25/2018, 10/6/2018, 10/9/2018, 10/14/2018, 10/17/2018
WV3	9/7/2014, 8/22/2015, 9/15/2015, 9/28/2015, 11/24/2015, 3/4/2016, 6/20/2016, 7/21/2016, 8/21/2016, 10/3/2016, 10/10/2016, 5/8/2017, 7/23/2017, 7/28/2017, 8/4/2017, 8/22/2017, 9/10/2017, 9/17/2017, 10/17/2017, 10/30/2017, 3/4/2018, 3/16/2018, 3/17/2018, 4/5/2018, 4/23/2018, 4/24/2018, 8/8/2018, 8/14/2018, 8/21/2018, 8/27/2018, 9/8/2018, 10/15/2018, 10/16/2018

REFERENCES

- [1] C. S. R. Neigh, J. G. Masek, and J. E. Nickeson, "High-resolution satellite data open for government research," *Eos, Trans. Amer. Geophys. Union*, vol. 94, no. 13, pp. 121–123, Mar. 2013, doi: [10.1002/2013EO130002](https://doi.org/10.1002/2013EO130002).
- [2] M. Brandt et al., "An unexpectedly large count of trees in the West African Sahara and Sahel," *Nature*, vol. 587, no. 7832, pp. 78–82, Nov. 2020, doi: [10.1038/s41586-020-2824-5](https://doi.org/10.1038/s41586-020-2824-5).
- [3] C. Tucker et al., "Sub-continental-scale carbon stocks of individual trees in African drylands," *Nature*, vol. 615, no. 7950, pp. 80–86, Mar. 2023, doi: [10.1038/s41586-022-05653-6](https://doi.org/10.1038/s41586-022-05653-6).
- [4] S. Eckert, "Improved forest biomass and carbon estimations using texture measures from WorldView-2 satellite data," *Remote Sens.*, vol. 4, no. 4, pp. 810–829, Apr. 2012, doi: [10.3390/rs4040810](https://doi.org/10.3390/rs4040810).
- [5] R. Naidu, F. Muller-Karger, and M. McCarthy, "Mapping of benthic habitats in Komave, Coral Coast using WorldView-2 satellite imagery," in *Climate Change Management*. Berlin, Germany: Springer, 2018, pp. 337–355, doi: [10.1007/978-3-319-70703-7_18](https://doi.org/10.1007/978-3-319-70703-7_18).
- [6] L. Qi et al., "In search of floating algae and other organisms in global oceans and lakes," *Remote Sens. Environ.*, vol. 239, Mar. 2020, Art. no. 111659, doi: [10.1016/j.rse.2020.111659](https://doi.org/10.1016/j.rse.2020.111659).
- [7] D. J. Jacob et al., "Quantifying methane emissions from the global scale down to point sources using satellite observations of atmospheric methane," *Atmos. Chem. Phys.*, vol. 22, no. 14, pp. 9617–9646, Jul. 2022, doi: [10.5194/acp-22-9617-2022](https://doi.org/10.5194/acp-22-9617-2022).
- [8] E. Sánchez-García, J. Gorroño, I. Irakulis-Loitxate, D. J. Varon, and L. Guanter, "Mapping methane plumes at very high spatial resolution with the WorldView-3 satellite," *Atmos. Meas. Techn.*, vol. 15, no. 6, pp. 1657–1674, Mar. 2022, doi: [10.5194/amt-15-1657-2022](https://doi.org/10.5194/amt-15-1657-2022).
- [9] D. J. Varon et al., "Satellite discovery of anomalously large methane point sources from oil/gas production," *Geophys. Res. Lett.*, vol. 46, no. 22, pp. 13507–13516, Nov. 2019, doi: [10.1029/2019GL083798](https://doi.org/10.1029/2019GL083798).
- [10] K. S. Krause, "QuickBird relative radiometric performance and on-orbit long term trending," in *Proc. SPIE Earth Observing Syst. XI*, 2006, Art. no. 62960P, doi: [10.1117/12.679693](https://doi.org/10.1117/12.679693).
- [11] K. S. Krause, "WorldView-1 pre and post-launch radiometric calibration and early on-orbit characterization," in *Proc. SPIE Earth Observing Syst. XIII*, 2008, Art. no. 708116, doi: [10.1117/12.794340](https://doi.org/10.1117/12.794340).
- [12] S. J. Cantrell et al., "System characterization report on the WorldView-3 imager," *U.S. Geol. Surv.*, 2021, doi: [10.3133/ofr20211030I](https://doi.org/10.3133/ofr20211030I).
- [13] D. R. Doelling et al., "The radiometric stability and scaling of collection 6 terra- and aqua-MODIS VIS, NIR, and SWIR spectral bands," *IEEE Trans. Geosci. Remote Sens.*, vol. 53, no. 8, pp. 4520–4535, Aug. 2015, doi: [10.1109/TGRS.2015.2400928](https://doi.org/10.1109/TGRS.2015.2400928).
- [14] T. Choi, C. Cao, S. Blonski, W. Wang, S. Upreti, and X. Shao, "NOAA-20 VIIRS reflective solar band postlaunch calibration updates two years in-orbit," *IEEE Trans. Geosci. Remote Sens.*, vol. 58, no. 11, pp. 7633–7642, Nov. 2020, doi: [10.1109/TGRS.2020.2982764](https://doi.org/10.1109/TGRS.2020.2982764).
- [15] I. V. Geogdzhayev and A. Marshak, "Calibration of the DSCOVR EPIC visible and NIR channels using MODIS Terra and aqua data and EPIC lunar observations," *Atmos. Meas. Techn.*, vol. 11, no. 1, pp. 359–368, Jan. 2018, doi: [10.5194/amt-11-359-2018](https://doi.org/10.5194/amt-11-359-2018).
- [16] C. M. Roithmayr et al., "CLARREO approach for reference intercalibration of reflected solar sensors: On-orbit data matching and sampling," *IEEE Trans. Geosci. Remote Sens.*, vol. 52, no. 10, pp. 6762–6774, Oct. 2014, doi: [10.1109/TGRS.2014.2302397](https://doi.org/10.1109/TGRS.2014.2302397).
- [17] C. Lukashin, B. A. Wielicki, D. F. Young, K. Thome, Z. Jin, and W. Sun, "Uncertainty estimates for imager reference intercalibration with CLARREO reflected solar spectrometer," *IEEE Trans. Geosci. Remote Sens.*, vol. 51, no. 3, pp. 1425–1436, Mar. 2013, doi: [10.1109/TGRS.2012.2233480](https://doi.org/10.1109/TGRS.2012.2233480).
- [18] A. Lyapustin, Y. Wang, S. Korkin, and D. Huang, "MODIS collection 6 MAIAC algorithm," *Atmos. Meas. Techn.*, vol. 11, no. 10, pp. 5741–5765, Oct. 2018, doi: [10.5194/amt-11-5741-2018](https://doi.org/10.5194/amt-11-5741-2018).
- [19] A. Lyapustin et al., "Scientific impact of MODIS C5 calibration degradation and C6+ improvements," *Atmos. Meas. Techn.*, vol. 7, no. 12, pp. 4353–4365, 2014, doi: [10.5194/amt-7-4353-2014](https://doi.org/10.5194/amt-7-4353-2014).
- [20] A. Lyapustin et al., "Calibration of the SNPP and NOAA 20 VIIRS sensors for continuity of the MODIS climate data records," *Remote Sens. Environ.*, vol. 295, Sep. 2023, Art. no. 113717, doi: [10.1016/j.rse.2023.113717](https://doi.org/10.1016/j.rse.2023.113717).
- [21] C. S. R. Neigh, J. McCorkel, and E. M. Middleton, "Quantifying Libya-4 surface reflectance heterogeneity with WorldView-1, 2 and EO-1 Hyperion," *IEEE Geosci. Remote Sens. Lett.*, vol. 12, no. 11, pp. 2277–2281, Aug. 2015, doi: [10.1109/LGRS.2015.2468174](https://doi.org/10.1109/LGRS.2015.2468174).
- [22] B. J. Russell et al., "The ground to space CALibration experiment (G-SCALE): Simultaneous validation of UAV, airborne, and satellite imagers for earth observation using specular targets," *Remote Sens.*, vol. 15, no. 2, Jan. 2023, Art. no. 294, doi: [10.3390/rs15020294](https://doi.org/10.3390/rs15020294).

- [23] D. Helder et al., "Observations and recommendations for coordinated calibration activities of government and commercial optical satellite systems," *Remote Sens.*, vol. 12, no. 15, Aug. 2020, Art. no. 2468, doi: [10.3390/RS12152468](https://doi.org/10.3390/RS12152468).
- [24] A. Lyapustin, Y. Wang, I. Laszlo, and S. Korkin, "Improved cloud and snow screening in MAIAC aerosol retrievals using spectral and spatial analysis," *Atmos. Meas. Techn.*, vol. 5, no. 4, pp. 843–850, 2012, doi: [10.5194/amt-5-843-2012](https://doi.org/10.5194/amt-5-843-2012).
- [25] T. Hilker, A. I. Lyapustin, C. J. Tucker, P. J. Sellers, F. G. Hall, and Y. Wang, "Remote sensing of tropical ecosystems: Atmospheric correction and cloud masking matter," *Remote Sens. Environ.*, vol. 127, pp. 370–384, Dec. 2012, doi: [10.1016/j.rse.2012.08.035](https://doi.org/10.1016/j.rse.2012.08.035).
- [26] M. J. Cooper, R. V. Martin, A. I. Lyapustin, and C. A. McLinden, "Assessing snow extent data sets over North America to inform and improve trace gas retrievals from solar backscatter," *Atmos. Meas. Techn.*, vol. 11, no. 5, pp. 2983–2994, 2018, doi: [10.5194/amt-11-2983-2018](https://doi.org/10.5194/amt-11-2983-2018).
- [27] A. Lyapustin, F. Zhao, and Y. Wang, "A comparison of multi-angle implementation of atmospheric correction and MOD09 daily surface reflectance products from MODIS," *Front. Remote Sens.*, vol. 2, pp. 1–15, Dec. 2021, doi: [10.3389/frsen.2021.712093](https://doi.org/10.3389/frsen.2021.712093).
- [28] E. E. Maeda et al., "Consistency of vegetation index seasonality across the Amazon rainforest," *Int. J. Appl. Earth Observation Geoinformation*, vol. 52, pp. 42–53, Oct. 2016, doi: [10.1016/j.jag.2016.05.005](https://doi.org/10.1016/j.jag.2016.05.005).
- [29] V. S. Martins, A. Lyapustin, L. A. S. De Carvalho, C. C. F. Barbosa, and E. M. L. M. Novo, "Validation of high-resolution MAIAC aerosol product over South America," *J. Geophys. Res.*, vol. 122, no. 14, pp. 7537–7559, 2017, doi: [10.1002/2016JD026301](https://doi.org/10.1002/2016JD026301).
- [30] V. S. Martins et al., "Global validation of columnar water vapor derived from EOS MODIS-MAIAC algorithm against the ground-based AERONET observations," *Atmos. Res.*, vol. 225, no. 0169-8095, pp. 181–192, 2019, doi: [10.1016/j.atmosres.2019.04.005](https://doi.org/10.1016/j.atmosres.2019.04.005).
- [31] M. Choi et al., "Validation, comparison, and integration of GOCI, AHI, MODIS, MISR, and VIIRS aerosol optical depth over East Asia during the 2016 KORUS-AQ campaign," *Atmos. Meas. Tech.*, vol. 12, no. 8, pp. 4619–4641, Aug. 2019, doi: [10.5194/amt-12-4619-2019](https://doi.org/10.5194/amt-12-4619-2019).
- [32] N. Schutgens et al., "An AeroCom-AeroSat study: Intercomparison of satellite AOD datasets for aerosol model evaluation," *Atmos. Chem. Phys.*, vol. 20, no. 21, pp. 12431–12457, Oct. 2020, doi: [10.5194/acp-20-12431-2020](https://doi.org/10.5194/acp-20-12431-2020).
- [33] B. N. Holben et al., "AERONET—A federated instrument network and data archive for aerosol characterization," *Remote Sens. Environ.*, vol. 66, no. 1, pp. 1–16, 1998, doi: [10.1016/S0034-4257\(98\)00031-5](https://doi.org/10.1016/S0034-4257(98)00031-5).
- [34] E. F. Vermote and S. Kotchenova, "Atmospheric correction for the monitoring of land surfaces," *J. Geophys. Res. Atmos.*, vol. 113, no. 23, Dec. 2008, doi: [10.1029/2007JD009662](https://doi.org/10.1029/2007JD009662).
- [35] D. Krutz et al., "The instrument design of the DLR earth sensing imaging spectrometer (DESI)," *Sensors*, vol. 19, no. 7, Apr. 2019, Art. no. 1622, doi: [10.3390/s19071622](https://doi.org/10.3390/s19071622).
- [36] K. Alonso et al., "Data products, quality and validation of the DLR earth sensing imaging spectrometer (DESI)," *Sensors*, vol. 19, no. 20, Oct. 2019, Art. no. 4471, doi: [10.3390/s19204471](https://doi.org/10.3390/s19204471).
- [37] A. I. Lyapustin, "Radiative transfer code SHARM for atmospheric and terrestrial applications," *Appl. Opt.*, vol. 44, no. 36, Dec. 2005, Art. no. 7764, doi: [10.1364/AO.44.007764](https://doi.org/10.1364/AO.44.007764).
- [38] S. Korkin and A. Lyapustin, "Matrix exponential in C/C++ version of vector radiative transfer code IPOL," *J. Quantitative Spectrosc. Radiative Transfer*, vol. 227, pp. 106–110, 2019, doi: [10.1016/j.jqsrt.2019.02.009](https://doi.org/10.1016/j.jqsrt.2019.02.009).
- [39] A. I. Lyapustin et al., "Multi-angle implementation of atmospheric correction for MODIS (MAIAC): 3. Atmospheric correction," *Remote Sens. Environ.*, vol. 127, pp. 385–393, Dec. 2012, doi: [10.1016/j.rse.2012.09.002](https://doi.org/10.1016/j.rse.2012.09.002).
- [40] W. Lucht, C. B. Schaaf, and A. H. Strahler, "An algorithm for the retrieval of albedo from space using semiempirical BRDF models," *IEEE Trans. Geosci. Remote Sens.*, vol. 38, no. 2, pp. 977–998, Mar. 2000, doi: [10.1109/36.841980](https://doi.org/10.1109/36.841980).
- [41] X. Xiong et al., "MODIS AND VIIRS calibration and characterization in support of producing long-term high-quality data products," *Remote Sens.*, vol. 12, no. 19, pp. 1–28, Oct. 2020, doi: [10.3390/rs12193167](https://doi.org/10.3390/rs12193167).
- [42] J. Sun, X. Xiong, A. Angal, H. Chen, A. Wu, and X. Geng, "Time-dependent response versus scan angle for MODIS reflective solar bands," *IEEE Trans. Geosci. Remote Sens.*, vol. 52, no. 6, pp. 3159–3174, Jun. 2014, doi: [10.1109/TGRS.2013.2271448](https://doi.org/10.1109/TGRS.2013.2271448).
- [43] A. Angal et al., "On-orbit calibration of terra MODIS VIS bands using polarization-corrected desert observations," *IEEE Trans. Geosci. Remote Sens.*, vol. 58, no. 8, pp. 5428–5439, Aug. 2020, doi: [10.1109/TGRS.2020.2966000](https://doi.org/10.1109/TGRS.2020.2966000).
- [44] L. G. Tilstra, O. N. E. Tuinder, P. Wang, and P. Stammes, "Surface reflectivity climatologies from UV to NIR determined from earth observations by GOME-2 and SCIAMACHY," *J. Geophys. Res. Atmos.*, vol. 122, no. 7, pp. 4084–4111, Apr. 2017, doi: [10.1002/2016JD025940](https://doi.org/10.1002/2016JD025940).
- [45] O. Coddington, J. L. Lean, P. Pilewskie, M. Snow, and D. Lindholm, "A solar irradiance climate data record," *Bull. Amer. Meteorological Soc.*, vol. 97, no. 7, pp. 1265–1282, 2016, doi: [10.1175/BAMS-D-14-00265.1](https://doi.org/10.1175/BAMS-D-14-00265.1).
- [46] D. R. Doelling, D. Morstad, B. R. Scarino, R. Bhatt, and A. Gopalan, "The characterization of deep convective clouds as an invariant calibration target and as a visible calibration technique," *IEEE Trans. Geosci. Remote Sens.*, vol. 51, no. 3, pp. 1147–1159, Mar. 2013, doi: [10.1109/TGRS.2012.2225066](https://doi.org/10.1109/TGRS.2012.2225066).
- [47] R. Bhatt et al., "Response versus scan-angle assessment of MODIS reflective solar bands in collection 6.1 calibration," *IEEE Trans. Geosci. Remote Sens.*, vol. 58, no. 4, pp. 2276–2289, Apr. 2020, doi: [10.1109/TGRS.2019.2946963](https://doi.org/10.1109/TGRS.2019.2946963).
- [48] C. Cao, M. Weinreb, and H. Xu, "Predicting simultaneous nadir overpasses among polar-orbiting meteorological satellites for the inter-satellite calibration of radiometers," *J. Atmospheric Ocean. Technol.*, vol. 21, no. 4, pp. 537–542, Apr. 2004, doi: [10.1175/1520-0426\(2004\)021<0537:PSNOAP>2.0.CO;2](https://doi.org/10.1175/1520-0426(2004)021<0537:PSNOAP>2.0.CO;2).
- [49] M. Chu, J. Sun, and M. Wang, "Performance evaluation of on-orbit calibration of SNPP VIIRS reflective solar bands via intersensor comparison with Aqua MODIS," *J. Atmospheric Ocean. Technol.*, vol. 35, no. 2, pp. 385–403, Feb. 2018, doi: [10.1175/JTECH-D-17-0008.1](https://doi.org/10.1175/JTECH-D-17-0008.1).
- [50] S. Upreti and C. Cao, "Suomi NPP VIIRS reflective solar band on-orbit radiometric stability and accuracy assessment using desert and Antarctica Dome C sites," *Remote Sens. Environ.*, vol. 166, pp. 106–115, Sep. 2015, doi: [10.1016/j.rse.2015.05.021](https://doi.org/10.1016/j.rse.2015.05.021).
- [51] D. P. Roy et al., "Multi-temporal MODIS-Landsat data fusion for relative radiometric normalization, gap filling, and prediction of Landsat data," *Remote Sens. Environ.*, vol. 112, no. 6, pp. 3112–3130, Jun. 2008, doi: [10.1016/j.rse.2008.03.009](https://doi.org/10.1016/j.rse.2008.03.009).



Myungje Choi received the Ph.D. degree in atmospheric sciences from Yonsei University, Seoul, South Korea, in 2017.

From 2017 to 2018, after graduation, he worked on developing and improving satellite aerosol retrieval algorithms and air quality studies as a Postdoctoral Fellow with Yonsei University and from 2018 to 2020, with the NASA Jet Propulsion Laboratory, California Institute of Technology. He is currently an Assistant Research Scientist with Goddard Earth Sciences Technology and Research II, University of Maryland, Baltimore County, Baltimore, MD, USA, and a co-op scientist with Climate and Radiation Laboratory, NASA Goddard Space Flight Center, Greenbelt, MD. His research interests include remote sensing of aerosols and radiometric calibration with multiple satellite missions, including EPIC, MODIS, VIIRS, geostationary, and commercial satellites.



Alexei Lyapustin received the Ph.D. degree in aerospace remote sensing from Space Research Institute, Moscow, Russia, in 1997.

Since 1997, he has been with GSFC, initially with USRA in 1997–1999, then with JCET and GEST UMBC in 1999–2011, and as a civil servant since 2011. He is currently a Physical Research Scientist with the Climate and Radiation Laboratory. His research interests include remote sensing of atmospheric aerosol and land surface environmental parameters (bidirectional reflectance and albedo, and snow properties including grain size, albedo and subpixel snow fraction) from polar-orbiting and geostationary sensors, analysis of field campaign data, and 1-D and 3-D radiative transfer theory with gaseous absorption and polarization.

Dr. Lyapustin is a Member of MODIS, VIIRS, PACE, and DSCOVR science teams.



Yujie Wang received the Ph.D. degree in geography from Boston University, Boston, MA, USA, in 2002.

He has actively contributed to several satellite missions, including MODIS, VIIRS, EPIC, PACE, AHI, and ABI. His work involves developing sophisticated scientific algorithms to retrieve critical environmental parameters, such as leaf area index, fraction of photosynthetically active radiation, surface reflectance, and aerosol properties. He also has expertise in cross-calibrating sensors to ensure consistent satellite data products. His extensive experience extends to satellite

data validation, which he accomplishes through rigorous data analysis and field campaigns. His research focuses on radiative transfer processes within both the atmosphere and vegetation.



Compton J. Tucker received the Ph.D. degree from the College of Forestry, Colorado State University, Fort Collins, CO, USA, in 1975.

From 2005 to 2010, he was on NASA detail to the U.S. Global Change Program where he was the co-chairperson of two Interagency Working Groups, for observations and for land use and land cover change. He was active in NASA's Space Archaeology Program and has conducted ground-based radar and magnetic surveys at Troy, the Granicus River Valley, and Gordion in Turkey, with the University of

Cincinnati and University of Pennsylvania projects working at these locations from 2001 to 2012. Since 2014, he has been active in mapping land and forest degradation and attempting to quantify arid and semi-arid woody biomass using Landsat, MODIS, and large volumes of commercial satellite data. He specializes in studying the Earth with satellite data. He was among the first researchers to employ coarse-resolution satellite data to exploit the time domain for studying global photosynthesis on land, determining land cover, monitoring droughts, providing famine early warning, and predicting ecologically coupled disease outbreaks. He has also used large quantities of Landsat data to study forest condition, deforestation, and forest fragmentation in temperate, subtropical, and tropical forests, and to study glacier extent.



Maudood N. Khan received the Ph.D. degree in Environmental Engineering from the Department of Civil and Environmental Engineering, the Georgia Institute of Technology, Atlanta, GA, USA, in 2003.

Between 2018 and 2020, he co-led the development and presentation to the Office of Management and Budget NASA response to the 2020 Federal civil-agency satellite needs survey, and through a pilot program helped establish on a sustained basis the Commercial Smallsat Data Acquisition Program. Last year, he supported a review of the Airborne In-

strument Technology Transition program, and the development of Earth science division modeling strategy. He is currently a Lead Scientist with Booz Allen Hamilton supporting the Associate Director for Research and Analysis program within the Earth Science Division with NASA headquarters, Washington, DC, USA. He has been in this role since 2018. The most significant among his current responsibilities is NASA's engagement with the Coordination Group for Meteorological Satellites that the Associate Director leads on behalf of the agency. Earlier in his career, he engaged extensively with policy makers and stakeholders within and outside the U.S. to highlight the value of synergistic use of spaceborne, ground-based observations and atmospheric models to understand and mitigate the risks to public health associated with air pollution and environmental degradation.



Frederick Policelli received the Ph.D. degree in Earth and Planetary Sciences from Earth and Planetary Sciences Department, Johns Hopkins University, Baltimore, MD, USA, in 2018.

He studied mechanical engineering and worked in propulsion systems development and testing during his early career. He has extensive experience in applied sciences, systems engineering, and project management. He is currently a Principal Investigator on a NASA mission concept development project and Co-Investigator on a NASA Applied Sciences funded project that develops near real time global to regional scale flood mapping products with the goal of extending the results to operational partners for use in disaster management. His research interests include research and applications including surface water and flood water mapping.

Dr. Policelli is a Member of the NASA GSFC Hydrological Sciences Laboratory.



Christopher S. R. Neigh received the Ph.D. degree in Geography from the Department of Geographical Sciences, University of Maryland, College Park, MD, USA, in 2008.

Since 2001, he has been with GSFC, initially with Science Systems Applications Inc. in 2001–2009, then a NASA Postdoctoral Fellow in 2009 and 2010, and a civil servant since 2010. He is currently the Landsat 8 and 9 Project Scientist and is a Co-lead of the Landsat Science Team. He has extensive experience quantifying land-cover land-use change, biomass, and modeled the terrestrial carbon-cycle with disturbance. His research interests include drivers of change to agriculture and forested ecosystems using a suite of multispectral sensors, synthetic aperture radar, spaceborne and airborne LiDAR, and very higher resolution commercial satellite data. He uses these remote sensing tools with machine learning and AI to characterize the productivity, type, structure, and carbon content of land surface vegetation.

Dr. Neigh is a Member of the GSFC Biospheric Sciences Laboratory.



Alfreda A. Hall received the Bachelor of Science degree in Mathematics from University of North Carolina, Greensboro, North Carolina, in 1982.

She was a Computer Engineer with NASA GSFC from 1982 to 2023 and a CSDA Project Manager with Earth Science Division, Science Mission Directorate, at both NASA HQ and NASA GSFC. In her role as CSDA Project Manager, she led the project's efforts to identify, evaluate, acquire, and manage data from commercial sources, crucial for supporting NASA's Earth science research and applications. She also

contributed to Earth science data through the Earth Observing System Data and Information System of several satellite missions, including SNPP, JPSS-1, etc. Furthermore, She actively mentored interns involved in NASA's Earth Science Data and Information System Project.